2011

Measurement of ultra-thin film fracture by nano-indentation: a numerical study

Benjamin A. Burke
Iowa State University

Measurement of ultra thin film fracture toughness by nano-indentation:

a numerical study

by

Benjamin Burke

A thesis submitted to the graduate faculty

in partial fulfillment of the requirements for the degree of

MASTERS OF SCIENCE

Major: Engineering Mechanics

Program of Study Committee:
Wei Hong, Co-Major Professor
Ashraf Bastawros, Co-Major Professor
Valery Levitas

Iowa State University

Ames, Iowa

2011

Table of Contents

List of Figures

Table of Tables

Abstract

As the individual layers of interconnect structures decrease in size, it becomes increasingly difficult to determine the fracture toughness, and hence the reliability, of these layers. After a layer is thinner than ~500nm, it becomes difficult to determine the fracture toughness directly with traditional methods. Using nano-indentation, it is possible to extract the cohesive and adhesive fracture energies of these films without elaborate experimental setups. There are, however, several issues with this approach. Nano-indentation creates cracks both within the film (the cohesive cracks) and between the film and the substrate (the adhesive cracks) as well as significant plastic deformation of the film and substrate. Using SIMULA Abaqus Standard, a commercial finite element analysis tool, 2D and 3D models were created to examine the deformation characteristics associated with the nano-indentation process. The models either have pre-existing stationary cracks, or simulated by cohesive zone surfaces to account for crack nucleation and growth. The 2D model is axi-symmetric and only accounts for the adhesive crack. It is used primarily as a test the cohesive zone model and to begin to determine experimental testing limits. The 3D model is a one sixth slice of the area indented. Both cohesive and adhesive cracks are modeled and the interaction between the two cracks is investigated. While there are many parameters controlling the crack initiation and propagation process, several trends were identified. The domain of practical testing should be between one and three film thickness, so as to avoid the confluence of the indenter plastic process zone on the propagating crack front. When excursion on the load-indentation depth happens, the fracture energy is about 20% of the associated work done by the indenter (or the area under the excursion segment). The FEM simulation showed the general role of film thickness, toughness and modulus on the initiation and propagation of both cohesive and adhesive cracks. Though, there remains to be many other geometric attributes of the thin film fracture process that requires additional investigations.

Chapter 1) Introduction

The fracture toughness of ultra-thin films, i.e. films thinner than 500 nm, is of great interest to packaging and device reliability in microelectronics engineering. Nano-indentation has been used to find the fracture toughness of ultra-thin films without prior sample preparation (1) (2). It has been shown that for diamond-like films (films much harder than their substrate) the total acoustic energy emitted during indentation can be used to estimate crack length and greatly decrease the time needed to perform a nano-indentation fracture toughness test (3). This study attempts to extend this result to general ultra-thin films. However, during indentation of most ultra-thin films, there are two types of cracks generated, delamination of the film from the substrate (the adhesive crack) and channel cracking in the film (the cohesive crack), compared to only delamination of the film in the hard, diamond-like film. There is also extensive plasticity generated in the film during indentation. These two phenomena necessitated the development of a numerical model of fracture during indentation to gain a better understand of the processes involved.

The thesis is set up in three parts. The first part is an overview of nano-indentation and develops the relevant theories necessary for this study. The second part is a review of fracture mechanics and how they apply to cohesive zone models, the modeling technique employed by the numerical model. The third part describes the various models developed and the results found by each.

Chapter 2) Utilization of Nano-Indentation to Study Fracture of thin Films

Introduction

Ever since Friedrich Mohs (4) compared the hardness of two materials by identifying which material would permanently scratch the other, scientists have been using indentation testing to study material properties. Indentation testing is simply poking a known material into an unknown material and recording the results. The variety of hardness tests now available are all refinements of this principle. Nano-indentation has two distinguishing characteristics from other hardness tests. The first is the length scale. Has the name implies, during nano-indentation, length is measured in nanometers compared to microns or millimeters. The second is in the determination of the area of contact between the indenter and the specimen. In most indentation tests, the resulting impression in the sample is large enough that the contact area can be directly measured. In nano-indentation, the residual impression is on the order of microns and thus too small for optical measurement. Contact area is instead measured by using the known indentation depth and indenter geometry to calculate the contact area. Nano-indentation is often called depth-sensing indentation because of this. (4)

Nano-indentation can be used to determine more than just hardness as well. Studies on material's elastic modulus and hardness (5) (6) (7) (8), visco-elastic properties (9), strain hardening (10), and fracture toughness (3) has been conducted. The underlying deformation mechanisms will be examined in the next section. A few complicating matters such as thermal drift, indenter geometry, and pile-up are also briefly discussed.

Principles of Nano-Indentation

In order to study indentation, the principles of contact mechanics must first be examined. Contact mechanics deal with the interaction of two solid objects. It is generally divided into elastic contact and elastic-plastic contact. A brief overview of these principles follows.

Elastic Contact Mechanics

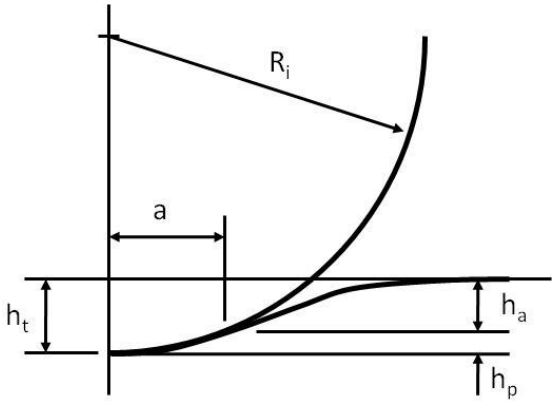

Figure 1: Schematic of contact between a spherical rigid indenter and a flat specimen (4)

Consider a rigid indenter of radius R_i in contact with a flat specimen as show in Figure 1. The contact radius a for an indenter load P can be found by (11)

$$a^3 = \frac{3}{4}\frac{PR}{E^*} \tag{2.1}$$

The reduced modulus, E^*, is a combination of the specimen's modulus and the indenter's modulus and can be found from

$$\frac{1}{E^*} = \frac{1-\nu^2}{E} + \frac{1-\nu'^2}{E'} \tag{2.2}$$

where the indenter's properties are primed.

In the limit of a semi-infinite specimen, the deformation, h, of the free surface is given by

$$h = \frac{3P}{8E^*a}\left(2 - \frac{r^2}{a^2}\right) \quad r \le a \tag{2.3}$$

It can be shown from Equation (2.3) that contact occurs at half of the total elastic displacement, i.e. $h_a = h_p = {}^{h_t}/_2$ (4).

The mean contact pressure, P_m, often referred to as the indentation stress, is given by the indenter load divided by the contact area,

$$P_m = \frac{P}{\pi a^2} \tag{2.4}$$

The mean contact pressure is often used as a normalizing parameter, as will be seen. Combining Equations (2.1) and (2.4) yields

$$P_m = \left(\frac{4E^*}{3\pi}\right)\frac{a}{R} \tag{2.5}$$

Since quantity a/R is often called the indentation strain, Equation (2.5) resembles the stress-strain response obtained from a conventional uniaxial tension test. It will be shown that more information about elastic-plastic properties are available from an indentation stress-strain response.

Now, consider a conical indenter as shown in Figure 2. The radius of contact a from a given indentation load P is given by (12)

$$P = \frac{\pi a}{2}\, E^* a \cot\alpha \tag{2.6}$$

and the deformation of the free surface is given by

$$h = \left(\frac{\pi}{2} - \frac{r}{a}\right) a \cot\alpha \quad r \le a \tag{2.7}$$

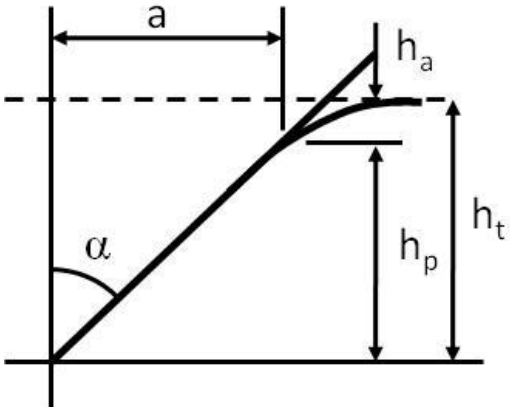

Figure 2: Schematic of contact between a conical rigid indenter and a flat specimen (4)

Contact occurs at h_p which is equal to the quantity $a \cot \alpha$. Combining Equation (2.6) and Equation (2.7) at $r = 0$ yields

$$P = \frac{2E^* \tan \alpha}{\pi} h_t^2 \tag{2.8}$$

with h_t being the total indentation depth of the indenter tip. The mean contact pressure for a conical indenter is again given by Equation (2.4). Combining Equation (2.4) and Equation (2.9) yields

$$P_m = \frac{1}{2} E^* \cot \alpha \tag{2.10}$$

which is constant for a given indenter and specimen. This means the indentation have geometric similarity and it is not possible to scale the indentation without external reference. This is dissimilar from a spherical indenter so care must be taken when using spherical indenters to maintain a constant indentation strain.

Elastic-Plastic Contact Mechanics

Indentation generally results in both elastic and plastic deformations. This caused considerable debate on the meaning of hardness. Early methods, such as the scratch test used by Mohs', involved too many variables to give a good meaning to hardness. It wasn't until Hertz postulated that hardness was the least

amount of pressure needed to produce a permanent indent at the center of the contact area that a manageable definition emerged. Later works have mostly been refinements of this idea.

It has been experimentally shown that the hardness number, H, is related to the mean contact pressure at which there is no increase with increasing indenter load. At this limit, the hardness number is given directly by the mean contact pressure for hardness methods that use the projected contact area such as nano-indentation. The specimen's yield stress, σ_Y, has been experimentally shown to be directly proportional to the hardness and can be expressed as

$$H \approx C\sigma_Y \tag{2.11}$$

where $C \approx 3$ for materials with a large ratio of E/σ_Y such as metals, and $C \approx 1.5$ for materials with a low ratio of E/σ_Y such as glass. A plot of the indentation stress over the indentation strain for a spherical indenter generally has three areas as summarized in Table 1.

Region	Response
$P_m < 1.1\sigma_Y$	Full elastic response
$1.1\sigma_Y < P_m < C\sigma_Y$	Plastic deformation exist but is constrained by surrounding elastic material. C is a constant based on material and indenter geometry
$P_m = C\sigma_Y$	Plastic region grows in size such that contact area increases without an increase of P_m

Table 1: Summary of the three regions generally found in an indentation stress-strain plot

Applications

Hardness and elastic modulus

Since a typical indentation has both elastic and plastic deformations, the calculations of the hardness and the elastic modulus of a specimen is not necessarily straight forward. Figure 3 shows a typical indenter

load versus displacement curve. Since there is only elastic deformation during unloading, the loading and unloading paths should be different, as can be seen. It can be shown that

$$S = \frac{dP}{dh} = 2E^* a \tag{2.12}$$

where S is the stiffness of the upper portion of the unloading data. Using the normal definition, hardness is found by

$$H = \frac{P_{max}}{\pi a^2} \tag{2.13}$$

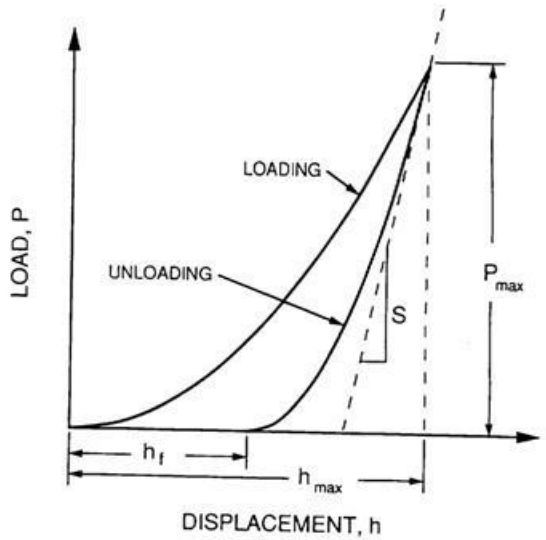

Figure 3: Schematic of a typical indenter load versus indenter displacement curve (5)

The main difficulty arises in trying to determine which contact radius, a, to use. The two obvious choices are the contact radius at the maximum indentation depth, h_{max}nd the contact radius at the final indentation depth, h_f. Another possibility, which yields better results than that other two, is to find a linear fit of the upper portion of the unloading curve and extrapolate, using the contact radius of the intercept. Even this contact radius has significant error as there is rarely any linearity in the unloading

curve due to a constant change in the contact area. The best, and most widely used method, was developed by Oliver and Pharr (5). It states that during unloading

$$h_p = h_{max} - h_a \tag{2.14}$$

where h_a is the depth at which the contact radius equals that in Equation (2.12) and Equation (2.13). For a conical indenter, it has been shown that (5)

$$h_a = \frac{2}{\pi}(\pi - 2)\frac{P}{S} \tag{2.15}$$

Since the contact radius of interest is at the peak load, Equation (2.15) becomes

$$h_a = \varepsilon \frac{P_{max}}{S} \tag{2.16}$$

where ε is an indenter geometry constant. For a conical indenter, $\varepsilon = 0.72$ and similar arguments show that $\varepsilon = 1$ for a flat punch and $\varepsilon = 0.75$ for a spherical indenter. The initial unloading stiffness, S, is found by fitting the unloading curve to a power law of the form

$$P = A\left(h - h_f\right)^m \tag{2.17}$$

with the constants A, h_f, and m found by a least squares fitting procedure. The initial unloading stiffness is then the derivative of Equation (2.17) with respect to h at $h = h_{max}$Equation (2.12) and Equation (2.13), along with the known tip geometry, can now be used to find the elastic modulus and hardness of the specimen.

Fracture toughness

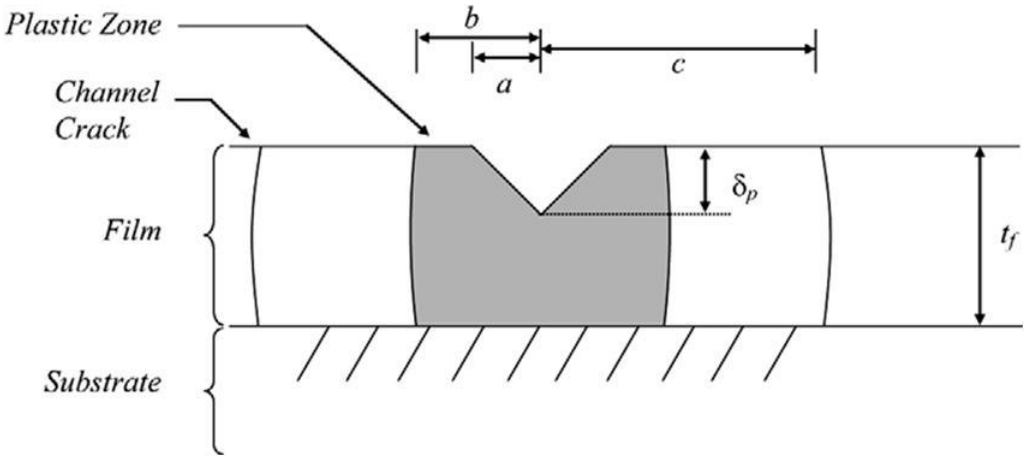

Figure 4: Schematic of channel cracking in a thin film (3)

Figure 4 illustrates channel cracking in a thin film during indentation. It can be shown that the fracture toughness of a channel crack in a thin film is given by (3)

$$K = \lambda \frac{\left(E_f H_f^2\right)^{\frac{1}{3}}}{t_f} \frac{a^2}{c^{\frac{1}{2}}} \tag{2.18}$$

where λ is a constant that depends on Poisson's ratio and indenter geometry. For most materials $\lambda \approx 0.013$ for a Vickers indenter and $\lambda \approx 0.016$ for a cube-corner indenter. Using the definition of hardness

$$H = \frac{P}{\eta a^2} \tag{2.19}$$

where η is an indenter shape constant for ideal tip geometries, Equation (2.18) can be rewritten as

$$K = \lambda' \left(\frac{E_f}{H_f}\right)^{\frac{1}{3}} \frac{1}{t_f} \frac{P}{c^{\frac{1}{2}}} \tag{2.20}$$

Generally, thin films contain a residual stress as a byproduct of manufacturing. This residual stress may act as either a crack driving or retarding force. It can be shown that the fracture toughness of a residual stress is given by

$$K = \psi' \sigma_R t_f^{\frac{1}{2}} \tag{2.21}$$

where ψ' is a constant that depends on the elastic mismatch between the film and substrate. Using linear superposition, Equations (2.20) and (2.21) are combined and the total stress intensity can be found from

$$K = \lambda' \left(\frac{E_f}{H_f}\right)^{\frac{1}{3}} \frac{1}{t_f} \frac{P}{c^{\frac{1}{2}}} + \psi' \sigma_R t_f^{\frac{1}{2}} \tag{2.22}$$

For thin film systems, the indenter usually indents completely through the film and into the substrate. To account for any plasticity in the film, a volume correction factor, V^*, given by

$$V^* = \begin{cases} 1, & h_f \leq t_f \\ 1 - \dfrac{\left(h_f - t_f\right)^3}{h_f^3}, & h_f > t_f \end{cases} \tag{2.23}$$

is used. Equation (2.22) is then rewritten as

$$K = \lambda' V^* \left(\frac{E_f}{H_f}\right)^{\frac{1}{3}} \frac{1}{t_f} \frac{P}{c^{\frac{1}{2}}} + \psi' \sigma_R t_f^{\frac{1}{2}} \tag{2.24}$$

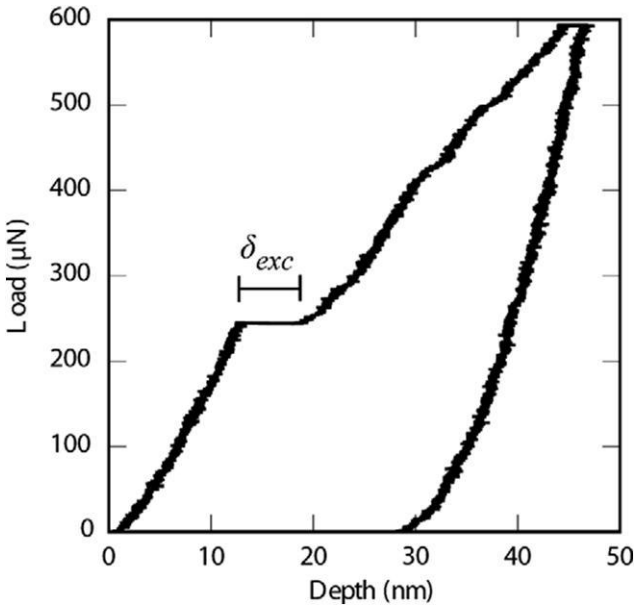

Figure 5: Load - displacement curve with an excursion (3)

During indentation, jumps in displacement, called excursions, sometimes occur. Figure 5 shows such an excursion. These excursions have been shown to have many sources, one of which is fracture. The total elastic energy released during an excursion can be approximated to the first order by integrating the area under the excursion (3), namely

$$U_{elastic} = P\delta_{exc} \tag{2.25}$$

Equation (2.25) assumes that that all energy released during an excursion is elastic energy and that there is no plastic dissipation.

Acoustic monitoring during nano-indentation tests have shown that there is often acoustic energy generated by rapid releases of elastic energy, such as during an excursion. The relationship between the total acoustic energy, ΣAE, and fracture toughness is given by

$$\Sigma AE = \alpha K_I t_f c \tag{2.26}$$

Rewriting Equation (2.26) to solve for crack length yields

$$c = \frac{1}{\alpha t_f K_I}\, \Sigma AE \tag{2.27}$$

Using the definition of linear elastic fracture toughness, K_I, and Equation (2.27), Equation (2.24) can be rewritten has

$$K = \lambda' V^* \left(\frac{E_f}{H_f}\right)^{\frac{1}{3}} \frac{1}{t_f} \frac{P}{\left(\frac{\Sigma AE}{\alpha t_f Y \sigma \pi^{\frac{1}{2}}}\right)^{\frac{1}{3}}} + \psi' \sigma_R t_f^{\frac{1}{2}} \tag{2.28}$$

Equation (2.28) allows for the estimation of fracture toughness of thin films with residual stress from the total acoustic energy released during indentation. This is highly useful as the measurement of crack length is the most time-consuming step in an indentation fracture toughness experiment.

Complicating Factors

Nano-indentation is not without its difficulties. There are several complicating factors that need to be taken into account when performing nano-indentation tests. Two of the most important are non-ideal indenter geometry and pile up or sink in of the specimen sample. Both of these affect the calculation of the contact area.

Non-Ideal Indenter Geometry

Figure 6 shows a SEM micrograph of a cube corner indenter. One ambiguity is the alignment of the cube corner axis with the indenter axis. The tip is often not in the center of the indenter, leading a varying included angle. Another issue is the sharpness of the indenter tip, wherein it is assumed to be infinitely sharp tip within the analytical framework. The indenter shown has a finite tip radius. This is due to the fact that it is impossible to manufacture an infinitely sharp tip. Moreover, the tip continually wears out during use. Therefore, a calibrated tip area function is constructed for each tip

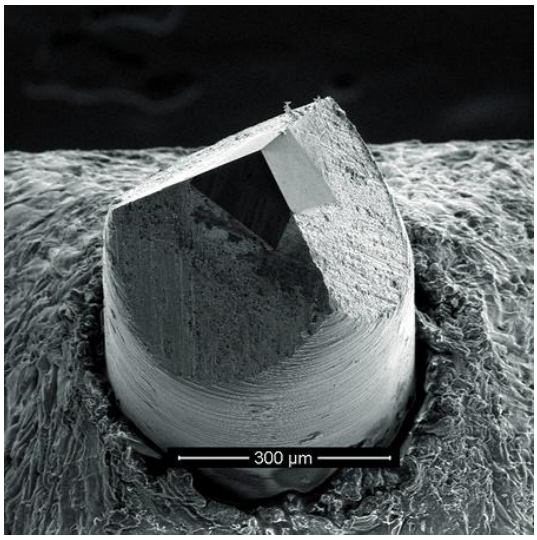

Figure 6: SEM micro graph of a cube corner indenter (13)

periodically. The most common method is to indent into a known material to several different depths. Rearranging Equation (2.12) to solve for the contact radius

$$a = \frac{2E^*}{S} \tag{2.29}$$

and plotting versus indentation depth allows a curve, called the tip area function, to be generated. This process needs to be repeated often as the indenter is used to account for any wear on the indenter.

Pile-up and sink-in

During indentation, a specimen's surface near the contact can either pile-up or sink-in. Plastic deformation is the reason for this. For materials with a high ratio of E/σ_Y such as metals, the plastic zone is a hemisphere with a radius much larger than the radius of contact. Most of the plastic deformation occurs near the indenter causing the material further out, but still within the plastic zone, to pile-up next to the indenter. For materials with a low ratio of E/σ_Y such as glasses, the plastic zone is generally constrained within the boundary of the contact radius (5). Elastic deformations are spread over a larger distance and the surface is more likely to sink-in. This piling-up or sinking-in of the surface must be accounted for when calculating the area of contact. For a given depth, a surface with pile-up will have a larger contact area than expected while a surface with sink-in will have a smaller contact area.

Conclusion

Nano-indentation is simply an extension of standard indentation experiments into the nanometer range. Due to the small size of the residual indentations, contact area is indirectly measured from the indentation depth instead of directly measured as in conventional indentation tests. The principles of contact mechanics are the driving theory behind all indentation tests. Nano-indentation can be used to examine several material properties, including hardness, elastic modulus elastio-plastic material properties (e.g. strain hardening), and fracture toughness. The relevant background theories have been outlined. Two complicating factors, non-ideal indenter geometry and pile-up/sink-in, have also been briefly discussed.

Chapter 3) Fracture Mechanics and Cohesive Zone Models

Introduction

During indentation of thin film systems, delamination of the film from the substrate and channel cracking of the film occurs. The numerical indentation model must account for these fractures modes and their interactions. One method of modeling the fracture process is to replace the crack tip and the associated process zone with a cohesive zone surface. Cohesive zone models assume a nonlinear traction-separation law and can be used to define the material response near the crack tip. A brief overview of fracture mechanics is given, followed by the details of cohesive zone models.

Fracture Mechanics

For as long as man has made structures, fracture has been an issue. Before the Industrial Revolution, the primary building materials for large structures were stone and mortar. These materials are unreliable in tension so early engineers designed structures that were loaded in compression. This is why arches, which cause compressive stresses in structures, are the predominant shape in ancient architecture (14). With the Industrial Revolution, construction materials able to carry tensile stresses, such as iron and steel, became widely available. New structures were no longer required to be purely compressive and lead to the plethora of structure styles known today. This transition was not without failures, most famously the rupture of a molasses tank in Boston (15) and the Liberty ships of World War II (16). The failure of the Liberty ships spurred researchers at the Naval Research Laboratory to study fracture in detail and lead to the field of fracture mechanics as it is known today (14). Today, fracture mechanics are generally divided into two regimes depending on the amount of plasticity near the crack: linear elastic fracture mechanics where there is little plasticity and elastic-plastic fracture mechanics where plasticity is prevalent. Since the numerical model used in this study assumes linear elastic fracture mechanics, a brief overview of this regime follows.

Linear elastic fracture mechanics apply to materials obey Hooke's law and structures whose global behavior is linear elastic. While seemingly of little use, they are the foundation of all other fracture mechanics. A material fractures when the atomic bonds that hold a material together are broken. The theoretical cohesive strength (σ_c) of a material has been shown to be given by (14)

$$\sigma_c = \sqrt{\frac{E\gamma_s}{x_0}} \approx \frac{E}{\pi} \tag{3.1}$$

where E is the elastic modulus, γ_s is the surface energy per unit area, and x_0 is the atomic spacing. Experimental fracture strengths are typically three to four orders of magnitude below this value for brittle materials however. This discrepancy is caused by flaws within the material magnifying the stress locally. Inglis' study of elliptical holes in infinite flat plates, as shown in Figure 7, was the first to show quantitative evidence of stress concentrations (17). The stress concentration, k_t, at point A is given by

$$k_t = \frac{\sigma_A}{\sigma} = 1 + \frac{2a}{b} \tag{3.2}$$

For a circular hole, $a = b$ and Equation (2.2) becomes $k_t = 3.0$, a well-known result for circular holes. As the major axis increases relative to the minor axis, it is convenient to rewrite Equation (3.2) in terms of the radius of curvature, $\rho = b^2/a$

$$k_t = 1 + 2\sqrt{\frac{a}{\rho}} \tag{3.3}$$

As the elliptical hole becomes more crack-like, $a \gg b$ and Equation (3.3) can be further reduced to

$$k_t = 2\sqrt{\frac{a}{\rho}} \tag{3.4}$$

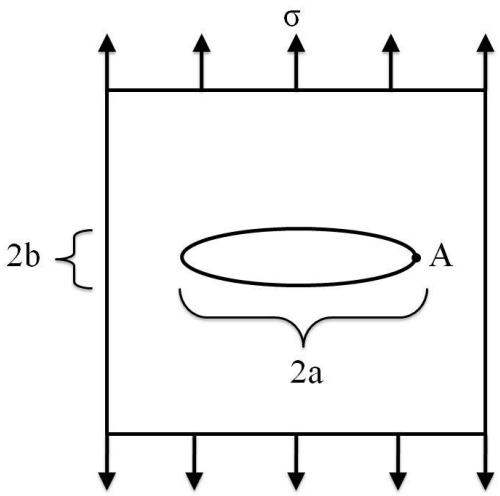

Figure 7: Elliptical hole in an infinite flat plate as used by Inglis and Griffith (if $a \gg b$)

Equation (3.4) initially caused concern when first published because, in the limit of an infinitely sharp crack, $\rho = 0$ and the stress concentration becomes infinity. Since no material can support infinite stress, any material containing a sharp crack should theoretically fail under even an infinitesimal load. However, no real material can contain an infinitely sharp crack. The minimum radius of curvature a crack tip can have is on the order of the atomic spacing, x_0. By substituting $\rho = x_0$ into Equation (2.4) and combining with Equation (2.1), a rough estimate (14) of the remote failure stress can be found by

$$\sigma_f = \sqrt{\frac{E\gamma_s}{4a}} \tag{3.5}$$

In order to avoid infinite stress at the crack tip, Griffith examined fracture from a potential energy standpoint (18). He applied the first law of thermodynamics, when a system goes from non-equilibrium to equilibrium there is a net decrease in energy, to crack formation and propagation. In this view, a crack can only form or propagate if the doing so causes the total energy, E, to decrease or remain constant. Consider an infinite plate of thickness B loaded with a through thickness crack as shown in Figure 7 with $a \gg b$. In order for an incremental increase of crack area, dA, under equilibrium conditions, enough

potential energy, Π, must be available to overcome the surface energy of the material,W_s. This energy balance can be expressed as (14)

$$\frac{dE}{dA} = \frac{d\Pi}{dA} + \frac{dW_s}{dA} = 0 \rightarrow -\frac{d\Pi}{dA} = \frac{dW_s}{dA} \tag{3.6}$$

Using the stress analysis of Inglis, the potential energy can be found by

$$\Pi = \Pi_0 - \frac{\pi\sigma^2 a^2 B}{E} \tag{3.7}$$

where Π_0 is the potential energy of the uncracked plate. Crack area in this example is given by $A = 2aB$ and the surface energy associated with this crack area by $W_s = 2aB\gamma_s$. However, there are two surfaces created during fracture so the total surface energy of the crack is given by

$$W_s = 4aB\gamma_s \tag{3.8}$$

Taking the derivatives of Equations (3.7) and (3.8) with respect to the crack area yields

$$\frac{d\Pi}{dA} = \frac{\pi\sigma^2 a}{E}, \frac{dW_s}{dA} = 2\gamma_s \tag{3.9}$$

Substituting Equation (3.9) into Equation (3.6) and solving for the remote fracture stress gives

$$\sigma_f = \sqrt{\frac{2E\gamma_s}{\pi a}} \tag{3.10}$$

This approach can be readily applied to other crack shapes. It can be shown that the remote fracture stress of an embedded penny-shaped flaw is given by

$$\sigma_f = \sqrt{\frac{\pi E \gamma_s}{2(1-\nu^2)a}} \tag{3.11}$$

where ν is the Poisson's ratio and a is the flaw radius.

Equation (3.10) is only valid in the limit of an ideally brittle material. In such material, stress is purely a linear response of strain. While this gives good agreement to experimental fracture strength of glass, it underestimates the fracture strength of metals. This is due to local plastic flow near the crack tip in metals that isn't accounted for in the Griffith energy balance. Irwin (19) proposed that the fracture energy, Γ, can be given by

$$\Gamma = 2\gamma_s + \gamma_p \tag{3.12}$$

where γ_p is the energy dissipated by any plastic, visco-elastic, or visco-plastic effects. Equation (3.10) can now be rewritten as

$$\sigma_f = \sqrt{\frac{E\Gamma}{\pi a}} \tag{3.13}$$

It should be noted that Equation (3.13) is only valid if all nonlinear, i.e. plastic, deformation is confined to a small region near the crack tip.

Irwin (20) also introduced the energy release rate, G, which is a measure of the energy available for crack propagation and is given by

$$G = -\frac{d\Pi}{dA} \tag{3.14}$$

Crack propagation occurs when the energy release rate reaches a critical value, G_c, which, by referring to Equation (3.6), can be found by

$$G_c = \frac{dW_s}{dA} = \Gamma \tag{3.15}$$

This critical energy release rate is a measure of the fracture toughness of the material.

The potential energy of an elastic body, Π, is defined as the difference between the stored strain energy, U, and the work done by external forces, W

$$\Pi = U - W \tag{3.16}$$

Consider a cracked plate loaded in load control as shown in Figure 8a. The stored strain energy and work, respectively, are given by

$$U = \int_0^{\Delta} P d\Delta = \frac{P\Delta}{2}, W = P\Delta \tag{3.17}$$

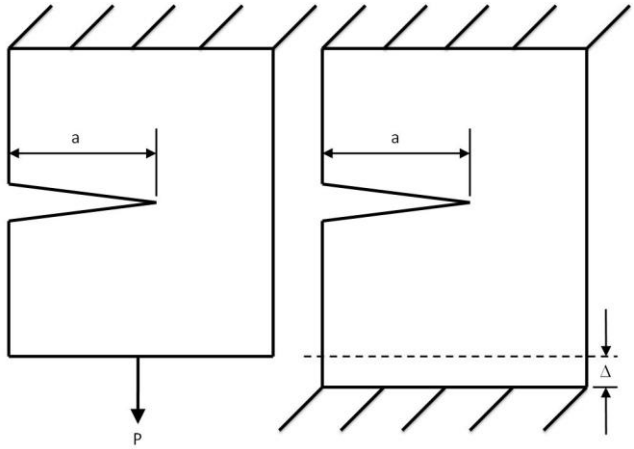

Figure 8: Sketch of a cracked plate loaded in a) load control and b) displacement control

Substituting Equation (3.17) into Equation (3.16) yields

$$\Pi = -U \tag{3.18}$$

For a though thickness crack in a plate of thickness B $A = aB$ and the energy release rate is given by

$$G = -\left(\frac{d\Pi}{dA}\right)_P = \left(\frac{da}{dA}\right)\left(\frac{dU}{d\Delta}\right)\left(\frac{d\Delta}{da}\right)_P = \frac{P}{2B}\left(\frac{d\Delta}{da}\right)_P \tag{3.19}$$

For a plate loaded in displacement control, as shown in Figure 8b, $W = 0$ therefore $\Pi = U$ and the energy release rate is given by

$$G = -\left(\frac{d\Pi}{dA}\right)_\Delta = -\left(\frac{da}{dA}\right)\left(\frac{dU}{dP}\right)\left(\frac{dP}{da}\right)_\Delta = -\frac{\Delta}{2B}\left(\frac{dP}{da}\right)_\Delta \tag{3.20}$$

By defining the compliance as the inverse of the stiffness, namely $C = \Delta/P$, Equations (3.19) and (3.20) become (14)

$$G = \frac{P^2}{2B}\frac{dC}{da} \tag{3.21}$$

This means that the energy release rate is the same for load control and displacement control. This allows the energy release rate to be determined in either method and be valid for all similar systems.

Figure 9 shows the three types of loading a crack can experience. In Mode I, the load is applied normal to the crack plane and tends to open the crack. In Mode II, the load is applied parallel to both the crack plane and direction of propagation and tends to slide one crack face along the other.

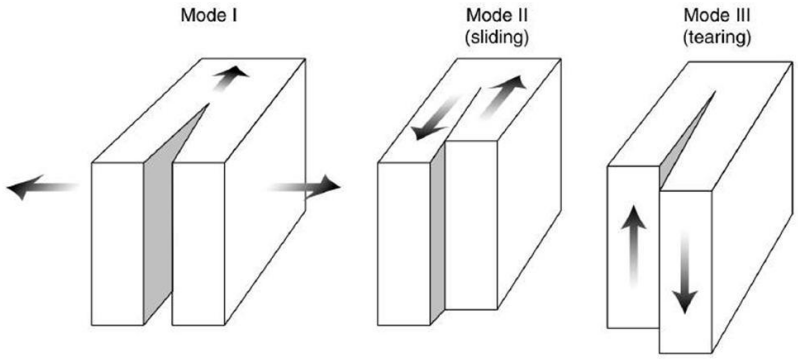

Figure 9: Sketch of the three fracture modes

In Mode III, the load is applied parallel to the crack plane and normal to the direction of propagation and tends to cause a tearing of the two crack faces. A crack can be loaded in any one of these modes or in a combination of two or all three modes.

It can be shown that the stress in the vicinity of the crack tip can be found by (14)

$$\sum_{n=I}^{III} \sigma_{ij}^{n} = \frac{K_n}{\sqrt{2\pi r}} f_{ij}^{n}(\theta) \tag{3.22}$$

where K_n is the stress intensity factor for a given mode, r is the distance ahead of the crack tip, and $f_{ij}^{n}(\theta)$ is dimensionless function of θ that depends on the mode. Since the stresses near the crack tip are all proportional to the stress intensity factor, if K can be determined from global behavior, it is possible to solve for all components of stress, strain, and displacement can be solved for an area near the crack tip known as the singularity-dominated zone. Analytical, numerical, and experimental research have shown that the stress intensity factor can be determined by (14)

$$K = Y\sigma\sqrt{\pi a} \tag{3.23}$$

where Y is a constant determined by crack shape and loading conditions, σ is the applied stress, and a is the characteristic crack length. For a through thickness crack loaded in Mode I, Equation (3.23) becomes

$$K_I = \sigma\sqrt{\pi a} \tag{3.24}$$

For linear elastic materials, the relationship between the energy release rate and the stress intensity factor are uniquely related. For a through thickness crack loaded in Mode I, the stress intensity factor is given by Equation (3.24) and the energy release rate by

$$G = \frac{\pi\sigma^2 a}{E} \tag{3.25}$$

Combining Equations (3.24) and (3.25), it can be found that

$$G = \frac{K_I^2}{E'} \tag{3.26}$$

where $E' = E$ for plane stress conditions and $E' = E/(1-\nu^2)$ for plain strain conditions. For a general cracking case, this relationship is given by (14)

$$G = \frac{K_I^2}{E'} + \frac{K_{II}^2}{E'} + \frac{K_{III}^2}{2\mu} \tag{3.27}$$

where μ is the shear modulus. It should be noted that Equation (3.27) assumes the crack remains planer and maintains a constant shape.

In real materials, there is a finite amount of yielding of the material near the crack tip. As long as this amount remains small, LEFM can be used but it must be taken into account. The normal stress ahead of the crack tip in a linear elastic material is given by (14)

$$\sigma_{yy} = \frac{K_I}{\sqrt{2\pi r}} \tag{3.28}$$

By assuming that yielding occurs when Equation (3.28) is equal to the yield stress of the material, a first approximation of the plastic zone size is given by

$$r_y = \frac{1}{2\alpha\pi}\left(\frac{K_I}{\sigma_Y}\right)^2 \tag{3.29}$$

where $\alpha = 1$ for plane stress conditions and $\alpha = 3$ for plane strain conditions. However, the material near the crack is no longer able to support the entire load that it previously held. This extra load would further increase the size of the plastic zone. A balance of forces near the crack tip leads to a second estimate for plastic zone size, r_p

$$\sigma_Y r_p = \int_0^{r_y} \frac{K_I}{\sqrt{2\pi r}} dr \rightarrow r_p = \frac{1}{\alpha\pi}\left(\frac{K_I}{\sigma_Y}\right)^2 \tag{3.30}$$

As long as $r_p \ll L$, where L is the characteristic length of the cracked body, LEFM can be used to determine the response of the cracked body.

Cohesive Zone Modeling

Cohesive zone models are a method of handling the localized inelastic processes associated with the extension of a crack. Cohesive zone models were first introduced by Barenblatt (22) and Dugdale (23) for ductile materials and by Hillerborg et al (24) for quasi-brittle materials. Cohesive zone models use a traction-separation law as shown in Figure 10. As the separation, Δ, between the top and bottom crack surfaces increases, the traction, T, the stress normal to these surfaces, increases linearly, similar to an elastic material. Once the cohesive strength of the material, σ_0, is reached, the ability of the material to hold stress begins to decrease. This simulates the strength reducing processes, small-scale yielding, micro-cracking, void nucleation, growth, and coalescence, etc. (25), that take place within the process zone. Once the separation reaches a critical value, δ_c, the material can no longer support any stress and the crack propagates. After the crack opening exceeds δ_c, the two material points connected by the cohesive zone is regarded as fully separated.

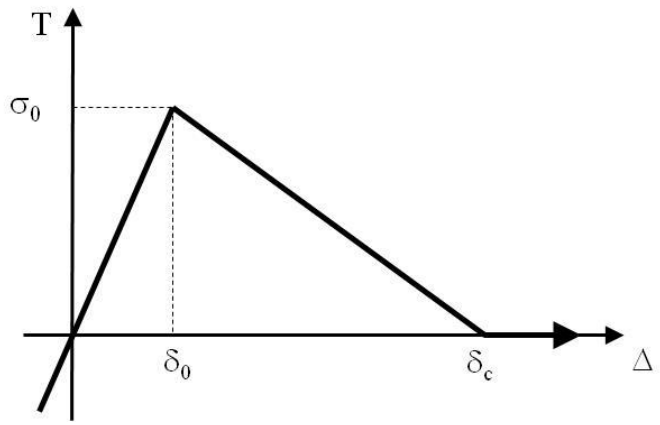

Figure 10: Sample bilinear traction-separation law used in the cohesive zone

By definition, the fracture energy of the material Γ is the area below the traction-separation curve, i.e. the work needed to create a unit area of fully developed crack:

$$\Gamma = \int_0^{\delta_c} T d\Delta \tag{3.33}$$

This implies that the cohesive zone model assumes all damage and inelastic deformation associated with fracture process are localized and any plasticity in the rest of the body is not directly related to fracture. This assumption causes difficulties when large plastic deformation is present near the crack tip, as will be discussed in the next chapter.

Various researchers have proposed many different forms for the traction-separation law, such as polynomial (22), step (23), exponential (26), and bilinear (27). It was assumed that the form of the traction-separation law was irrelevant and only the fracture energy and either the cohesive strength, σ_0, or the separation displacement, δ_0, needed to be known to completely define the cohesive zone. Recent research (28) suggests that the form, at least in quasi-brittle materials, does in fact matter. Chandra et al (27) compared experimental data from a thin slice push out to test cohesive zones with either a bilinear or exponential traction-separation law with constant fracture energy and cohesive strength and found that while the linear traction-separation law closely matches experimental data, the exponential traction-separation law yields a completely different response. Figure 11 summarizes their experimental and numerical results. This implies that care must be taken when using cohesive zone models to characterizes unknown materials.

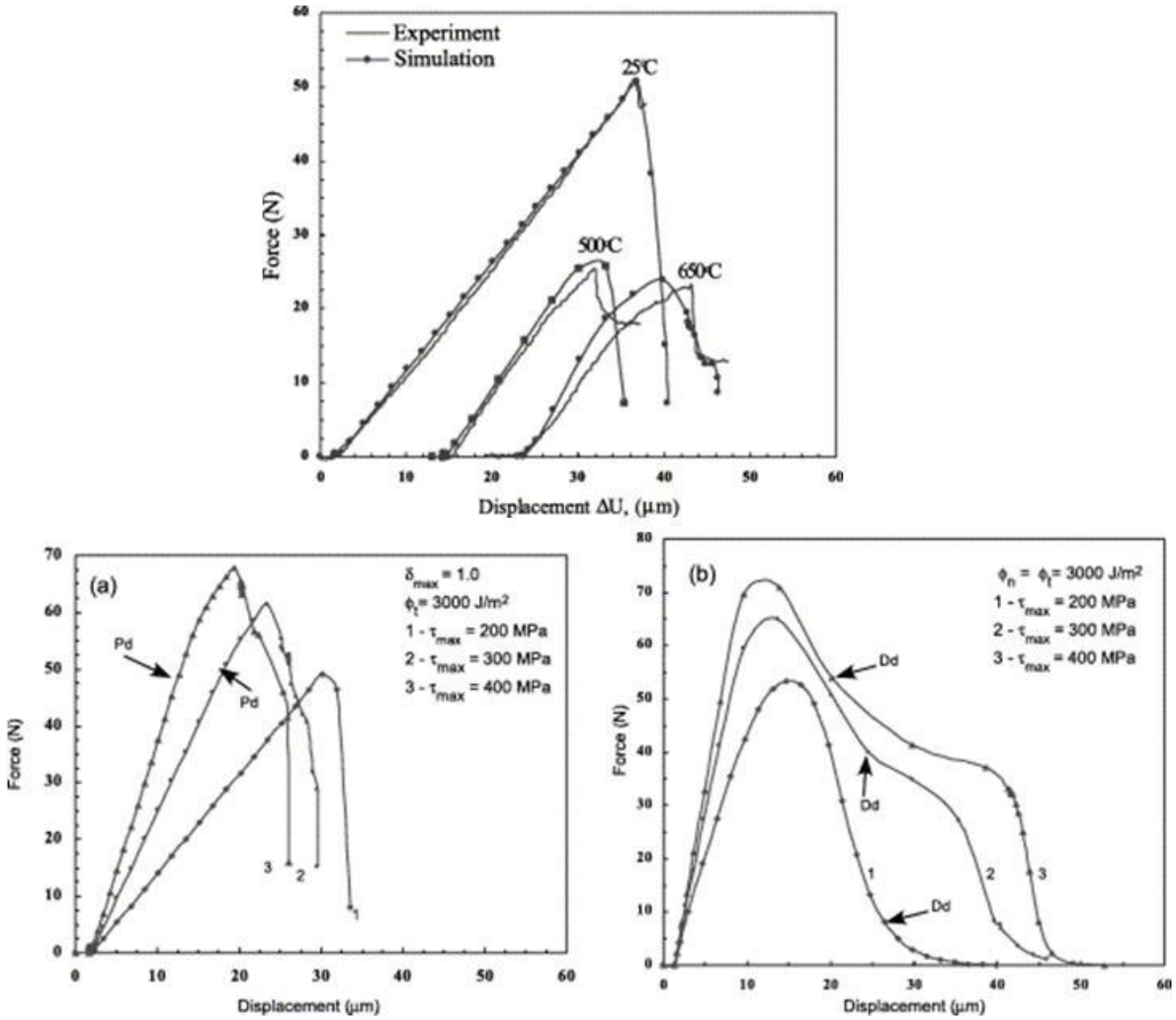

Figure 11: Force-displacement data for a) experimental results b) bilinear traction-separation law and c) exponential traction-separation law (28)

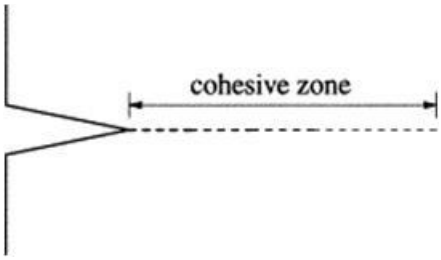

Figure 12: Schematic of cohesive zone ahead of the crack tip (25)

A cohesive zone model attempts to account for the process zone by collapsing the process zone into a line or a plane, depending on the number of model dimensions, ahead of the crack tip as shown in Figure 12. Along this line, elements with zero thickness are inserted into the surrounding continuum elements, as shown in Figure 13. Because of this, the fracture path must be known a priori. This is the biggest

limitation of cohesive zone models. The separation is defined as the resulting thickness of an element due to the deformation of the continuum.

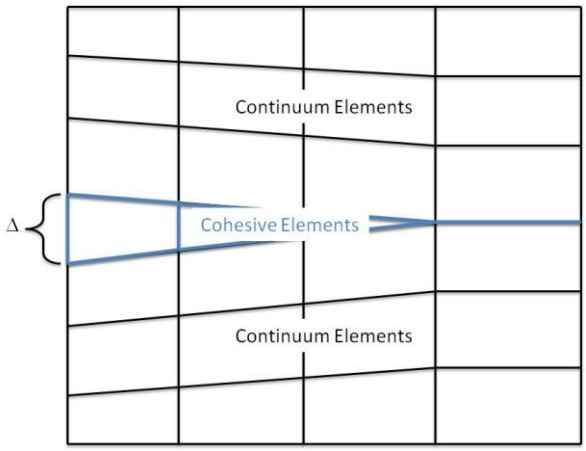

Figure 13: Schematic of cohesive elements inserted into a mesh of continuum elements with a partially opened crack

Since SIMULA Abaqus Standard is used to create the model used in this study, a brief overview of its cohesive zone model implementation is warranted. Abaqus describes the cohesive zone as a surface interaction between two bodies. These bodies are the structure in question divided along the fracture plane. Master and slave surfaces are designated. This designation is at the discretion of the user though the mesh of the slave surface should not be courser than the master surface. A traction-separation law is then used to describe the transfer of stress across this interface. The initial stiffness of the traction-separation law can either be defined by the user or Abaqus can estimate the stiffness as the elastic modulus of the slave surface. The initiation of softening can be defined in one of four ways given by

$$\max\left(<\frac{\sigma^I}{\sigma_0^I}>, \left|\frac{\sigma^{II}}{\sigma_0^{II}}\right|, \left|\frac{\sigma^{III}}{\sigma_0^{III}}\right|\right) \geq 1 \ (maximum\ stress)$$
$$\left(\frac{\sigma^I}{\sigma_0^I}\right)^2 + \left(\frac{\sigma^{II}}{\sigma_0^{II}}\right)^2 + \left(\frac{\sigma^{III}}{\sigma_0^{III}}\right)^2 \geq 1 \ (quadratic\ \ stress)$$
$$\max\left(<\frac{\delta^I}{\delta_0^I}>, \left|\frac{\delta^{II}}{\delta_0^{II}}\right|, \left|\frac{\delta^{III}}{\delta_0^{III}}\right|\right) \geq 1 \ (maximum\ displacement)$$
$$\left(\frac{\delta^I}{\delta_0^I}\right)^2 + \left(\frac{\delta^{II}}{\delta_0^{II}}\right)^2 + \left(\frac{\delta^{III}}{\delta_0^{III}}\right)^2 \geq 1 \ (quadratic\ displacement) \quad (3.34)$$

where the superscript denotes the fracture mode, σ_0 denotes the cohesive strength, δ_0 denotes the crack tip opening displacement associated with σ_0, σ the stress applied to the surface for a given mode, and δ the crack tip opening displacement in a given mode. The $< >$ brackets in the maximum stress and maximum displacement equations denotes

$$< x \geq \begin{cases} 0, x < 0 \\ x, x \geq 0 \end{cases} \tag{3.35}$$

The softening curve can then be defined as either linear or a power law. The fracture energy of the cohesive zone can either be given directly the user or the critical crack tip opening displacement given and the fracture energy calculated by Equation (3.33). Once the critical crack tip opening displacement is reached for a given element, the element is removed from the model and the surfaces treated as traction-free surfaces by Abaqus.

Conclusion

In conclusion, an overview of fracture mechanics has been given. Modern fracture mechanics are generally divided into two types, linear elastic fracture mechanics and elastic-plastic fracture mechanics, depending on the global material response. Cohesive zone models can be used to model crack propagation along a known path. They are able to do this by confining the fracture process zone into a line or plane of zero thickness elements along the path of fracture. These elements use a traction-separation law that decays after the cohesive strength limit of the material is reached. The fracture energy, cohesive strength limit, and, possibly, the form of the traction-separation law are needed to match the cohesive zone model to a given material.

Chapter 4: Modeling of Fracture Process during Nano-Indentation

Introduction

The fracture toughness of ultra-thin films is almost impossible to measure by non-indentation tests without extensive sample preparation (29). Nano-indentation has been used to find the fracture toughness of ultra-thin films without sample preparation (1) (2). In these experiments, the film-substrate system is indented and the force-displacement curves are recorded. The resulting indented surface is then scanned using atomic force microscopy (AFM) through which the resulting crack lengths can be determined. Figure 14 shows a typical AFM image. During indentation, there are two types of cracks generated: delamination of the film from the substrate (adhesive crack) and channel cracking in the film (cohesive crack). Since they are on the surface, cohesive cracks are the easier to see and measure. Their length can be taken directly from the AFM image. Adhesive cracks are much more difficult to measure. They are found by looking for an offset of the top surface of the film by at least one nanometer. Figure 15 shows a processed AFM image where the white area is the extent of delamination. The AFM imagine and measurement of crack lengths is the slowest step in a nano-indentation fracture toughness test. It has been shown that for diamond-like films, films much harder than their substrate, the total acoustic energy emitted during indentation can be used to estimate crack length and greatly decrease the time needed to perform a nano-indentation fracture toughness test (3).

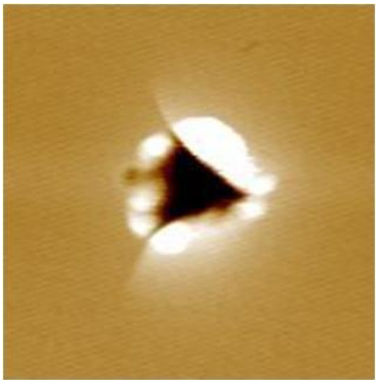

Figure 14: Typical AFM image

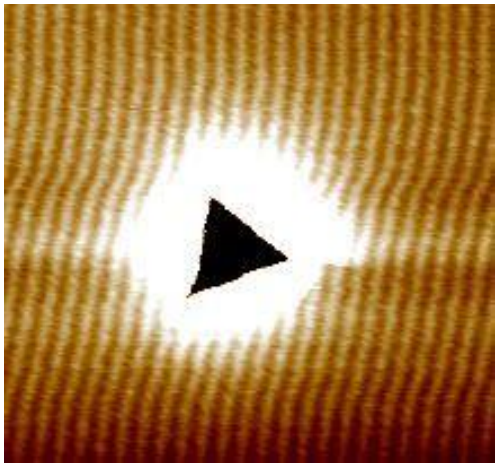

Figure 15: Processed AFM image showing delamination

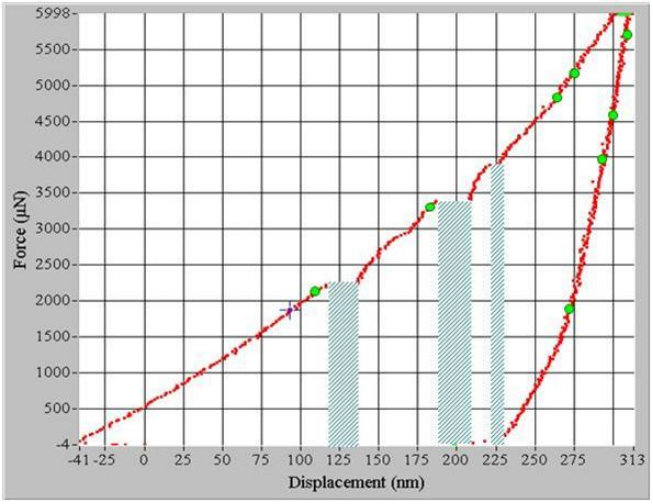

Figure 16: Typical experimental force - displacement curve, shaded regions under excursions are the work done by the indenter during fracture processes

Figure 16 shows a typical force-displacement curve. Several discontinuities, called excursions, can be observed on the loading curve. Each of them corresponds to an event of crack propagation. The area below the excursion of each discontinuity, shown as the shaded area on Figure 16, is the work done by the indenter in each event. Let δW be the work done by the indenter, δU_e be the increase in the elastic strain energy of the film-substrate system, δW_p be the plastic dissipation associated with the deformation during crack propagation, and δU_a and δU_c be the energy for extending the adhesive and cohesive cracks, respectively. Energy conservation dictates that

$$\delta W = \delta U_e + \delta W_p + \delta U_a + \delta U_c \tag{4.1}$$

All other irreversible energy loss, such as that carried by elastic waves, are either neglected or included in δW_p. If the fracture toughness can be assumed to be material constants, the energy terms δU_a and δU_c are directly related to the corresponding toughness as:

$$\delta U_a = \Gamma_a \delta a_a, \delta U_c = \Gamma_c \delta a_c \tag{4.2}$$

where Γ_a and Γ_c are the fracture toughness of the adhesive and cohesive cracks, respectively, and δa_a and δa_c are the corresponding increase in the crack areas in the event.

While δW can be measured directly from the load-displacement curve, the difficulty arises from the fact that there are at least four different packages of energy. Strictly speaking, the problem is indeterminate. However, since there is only one loading method – the indentation – and the events are associated with crack extension, it is believed that the different energy packages are strongly correlated. In this chapter, a numerical model is used to study the process and to gain insights towards the division of the four fracture-related energy packages.

Two Dimensional Model

A two dimensional (2D) axisymmetric model is created in Abaqus Standard. The axisymmetry limits the model to be applicable to adhesive cracks only. Eliminating one mode of cracking allowed for faster model development and shorter run times. Figure 17 shows a sketch of the model. The model is divided into three parts: a rigid indenter, a deformable film, and a deformable substrate with a cohesive surface between the film and substrate. Table 2 lists the material parameters of the film and substrate. To simplify the model, and to make it easier to convert to a different film –substrate system, the model dimensions are normalized by the film thickness (h) for all lengths and the yield stress

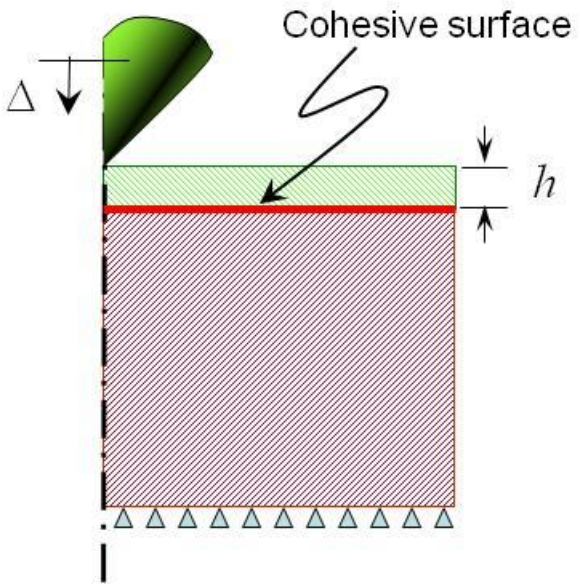

Figure 17: Sketch of 2D axisymmetric model

Indenter angle = 45°	Film	Film (non-dimensional)	Substrate	Substrate (non-dimensional)
Young's Modulus (E)	90 GPa	45.91	120 GPa	54.55
Poisson's Ratio (v)	0.3	0.3	0.3	0.3
Yield Stress (σ_Y)	2.2 GPa	1	2.2 GPa	1
Thickness	50 nm	1	5000 nm	100
Width	2500 nm	50	2500 nm	50

Table 2: Material properties and dimensions of the 2D model

of the film (σ_{Yf}) for all stresses. The film thickness is used as it is the only constant length scale. The yield stress of the film is chosen because the fracture process zone size of a crack can be estimated by fracture energy over the yield stress and the ratio of the elastic modulus to the yield stress is commonly examined. All other non-dimensional constants can be derived from these.

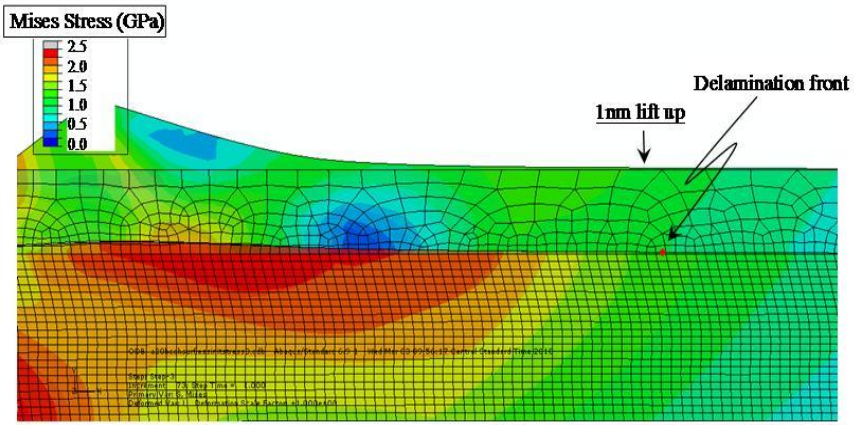

Figure 18: Extent of delamination compared to 1 nm lift up of top surface

First, the experimental method of determining the extent of delamination is verified. Figure 18 shows the deformed shape of an indented model after unloading. The location of one nanometer lift-up and the delamination front are marked. As can be seen, they are the same distance from the indention, thus verifying the method of crack-length measurement in experiments.

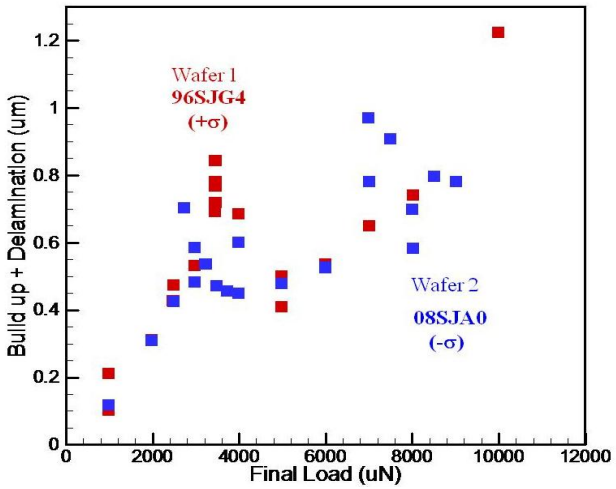

Figure 19: Experimental extent of delamination

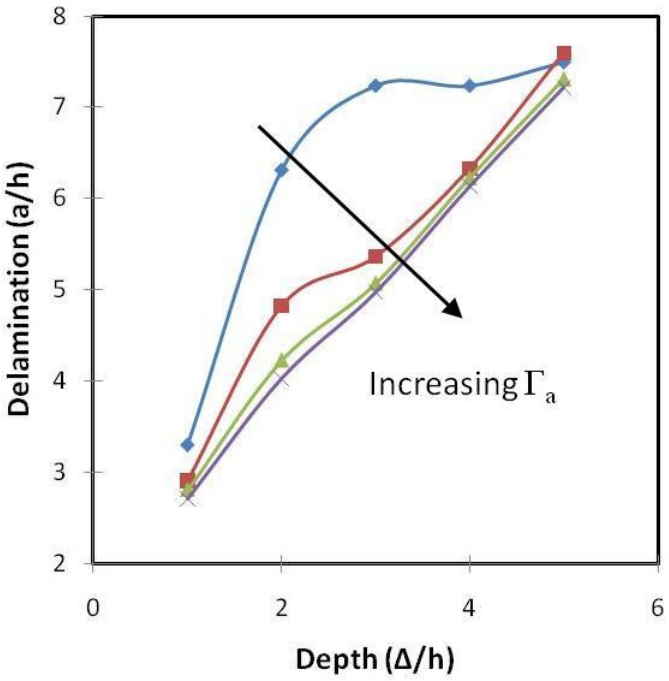

Figure 20: Delamination versus depth for various adhesive fracture energies

This 2D model is used to examine various limits of experimental measurements. Figure 19 shows the extent of delamination as determined from the experiment. As indentation depth increases, an increase in final load, delamination seems to propagate at one rate, stagnate for a period, and then propagate at a second rate. The first step to determine the experimental limits is to understand the reason for these changes in propagation rate. Figure 20 is the extent of delamination from the model for various fracture energies. They all generally follow the same trend as the experimental data. This implies that the numerical model can be used to determine the cause of the changing propagation rates. Figure 21 shows the von Mises stress in the film and substrate at different indentation depths. The gray region indicates the area at which the von Mises stress exceeds the yield strength, i.e. the plastic zone. The extent of delamination is marked on each figure as well. As shown in Figure 21a, the crack tip is well away from the large plastic deformation induced by indentation. In such a case, the inelastic effects related to fracture is fully characterized by the cohesive zone, and thus the parameters of the cohesive model can be used to identify the fracture toughness. As the depth increases, the plastic zone catches with and finally extends beyond the crack tip. Therefore, the fracture-related inelastic deformation is indistinguishable

from the indentation-induced large plastic deformation, and the fracture energy thus obtained is irrelevant to the fracture processes in an actual microelectronics device.

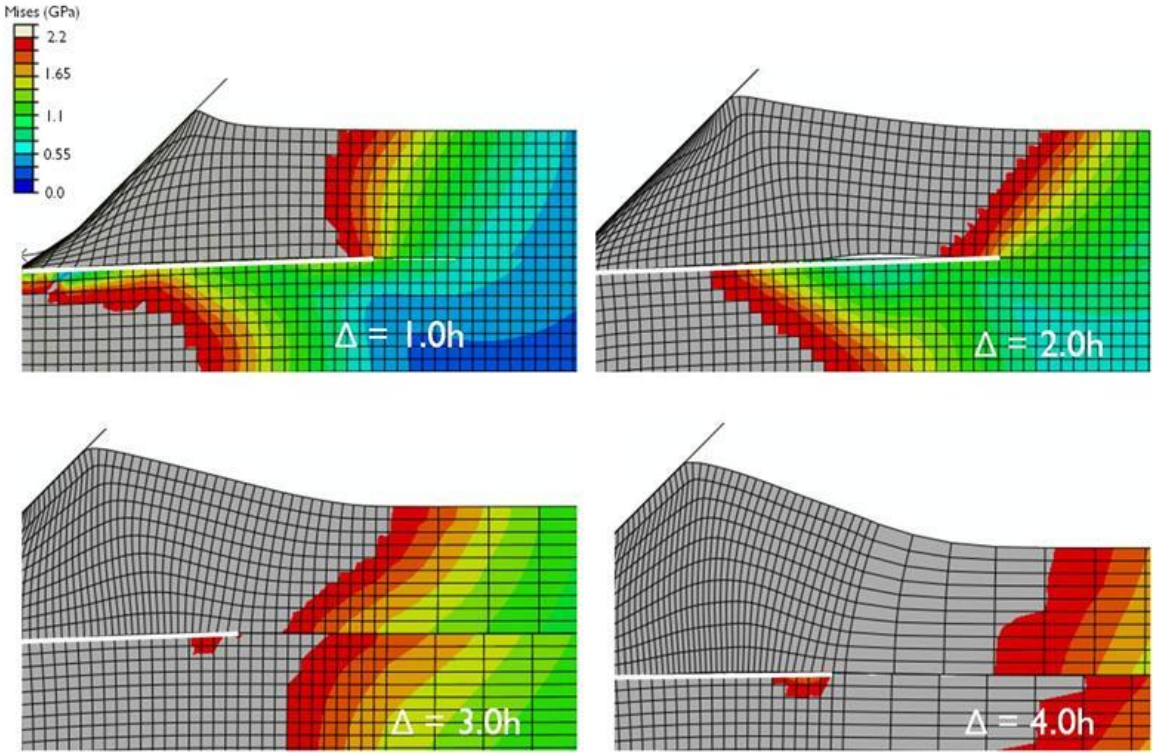

Figure 21: Area of large scale yielding (gray area) compared to delamination (what bar) a) $\Delta = 1.0h$ b) $\Delta = 2.0h$ c) $\Delta = 3.0h$ d) $\Delta = 4.0h$

The difference between these two regimes explains the changes in propagation rate. In the initial segment, the material's fracture energy is the dominant property and the delamination grows at the rate determined by the loading condition and the material property. Hence the different initial propagation rates are observed for models with different cohesive zone parameters in Figure 20. In the last segment, the indentation-induced plastic zone, which is determined by the overall geometry and the yield stress of the film, dominates the delamination process. Since the geometry and yield stress of the film are the same for all trials, they all propagate at the same rate. A transition is observed between the two regimes.

This leads to the first experimental limit: the crack must be longer than twice the indentation depth. Figure 22 shows the simulation results of the crack length (a) normalized by depth (Δ) versus the fracture energy (Γ) for various indentation depths. As depth increases, the effect of fracture energy diminishes,

i.e. the curves become flat. It is seen that this effect is most pronounced when $a/\Delta < 2$. Figure 23 shows the shear stress on the deformed shape for various depths. The crack tip is marked on each figure. Initially, the crack tip is far from the pile-up created by indentation. As depth increases, the pile-up, which is associated with large scale yielding, nears and eventually passes over the crack tip. The extent of pile-up is largely determined by the yield stress of the film and is consistently around twice the indentation depth for this system. Hence, the crack must be longer than twice the indentation depth to remain in the regime for meaningful fracture energy. Figure 24 shows the shear stress distributions when delamination initiates and at indentation depths $\Delta = 0.5h$, $\Delta = 0.75h$, and $\Delta = 1.0h$. The crack fronts are marked. As can be seen, delamination does not initiate at the center of the indentation but rather roughly under the intersection of the indenter and the top surface of the film. As indentation depth increases, the delamination propagates towards the center of the indentation as well as away from the indenter. This creates a torus shaped delamination area. Since the extent of delamination is measured by finding the location of one nanometer lift-up of the top surface and the inner radius of the delamination is under the residual indentation, it cannot be experimentally measured. This means that the indentation must be at least through the film thickness to insure that the area of delamination is circular. This then becomes the second experimental limit.

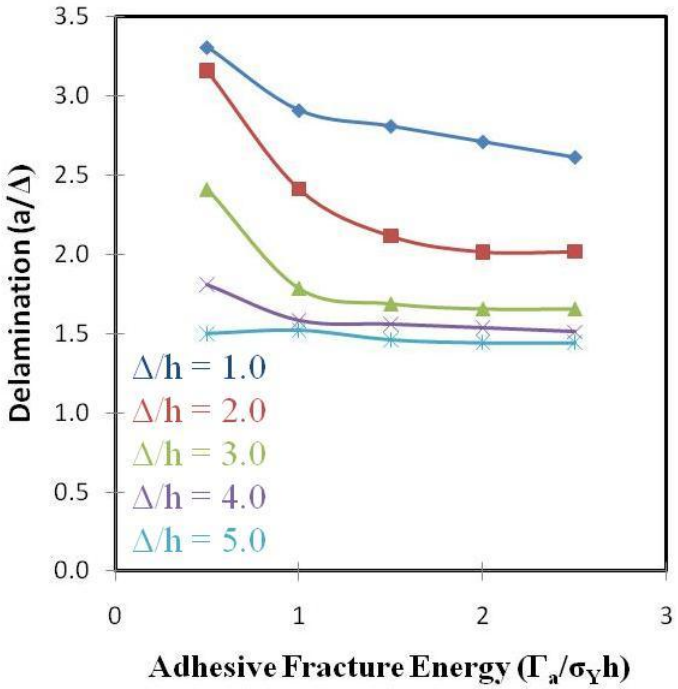

Figure 22: Delamination normalized by depth versus fracture energy for various depths

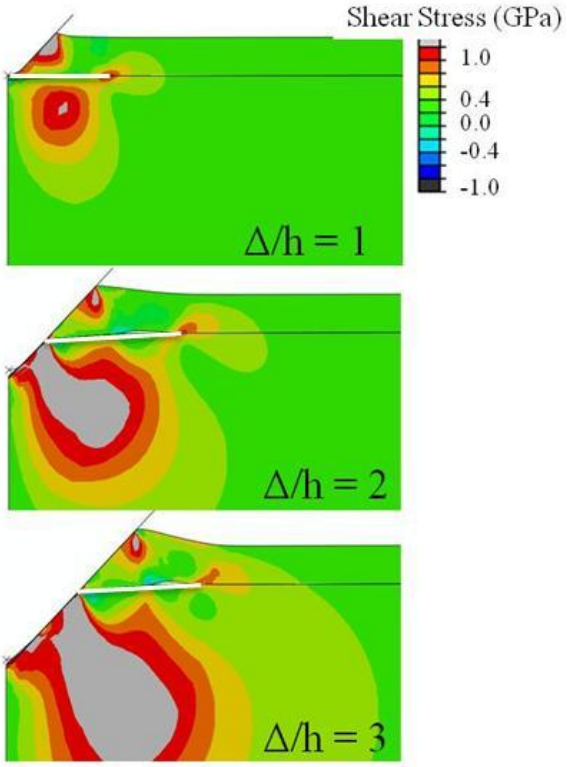

Figure 23: Shear stress profiles with delamination marked (white bar) at a) $\Delta = 1.0h$ b) $\Delta = 2.0h$ c) $\Delta = 3.0h$

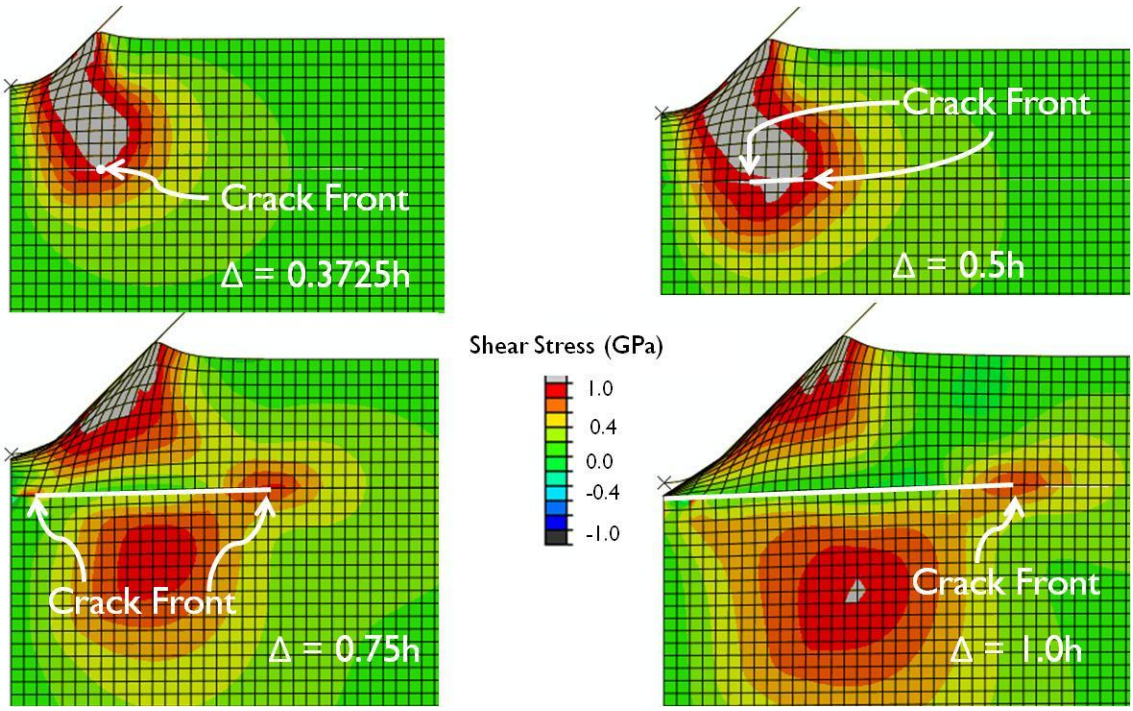

Figure 24: Shear stress with delamination marked (white bar) at a) delamination initiation ($\Delta = 0.3725h$) b) $\Delta = 0.5h$ c) $\Delta = 0.75h$ d) $\Delta = 1.0h$

Three Dimensional Model

Cohesive Zone Model

A three dimensional (3D) model is created in Abaqus Standard. Using the symmetry of the indenter, only one-sixth of the indentation is modeled. Figure 25 shows a sketch of the 3D model. Table 3 shows the material properties and dimensions used by the 3D model. The locations of the delamination and channel cohesive zones are marked. The outer half of the film-substrate interfaced is a perfect bond. The channel crack is constrained to the first half of the system with the remainder a symmetry boundary condition. This is done to reduce run time as neither crack ever extends beyond half the width of the model. The model is meshed using linear brick elements (C3D8) of one-fifth the film thickness a side in the area of the cohesive zones and to a depth of three times the film thickness from the surface of the film. The rest is meshed with an unstructured linear tetrahedral element (C3D4) refined in the direction of the structured mesh. This is done to insure a fine enough mesh in the area of the indentation and cracks while keeping the total number of elements low. The total depth of indentation was decreased from the five times the

film thickness used in the 2D model to twice the film thickness as in all deeper data the extent of delamination was less than twice the indentation depth.

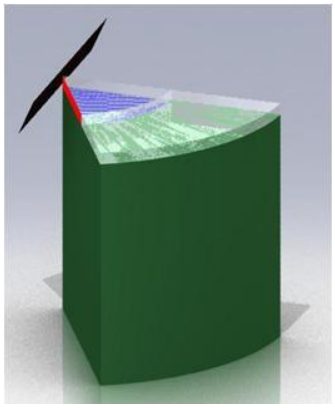

Figure 25: Sketch of the 3D model, red surface is the channel cohesive zone; blue surface is the adhesives cohesive zone

Cube Corner Indenter	Film	Film (non-dimensional)	Substrate	Substrate (non-dimensional)
Young's Modulus (E)	90 GPa	45.91	120 GPa	54.55
Poisson's Ratio (ν)	0.3	0.3	0.3	0.3
Yield Stress (σ_Y)	2.2 GPa	1	2.2 GPa	1
Thickness	50 nm	1	1000 nm	20
Width	1000 nm	20	1000 nm	20

Table 3: Material properties and dimensions for the 3D model

Since the film is relatively thin, the propagation of the channel crack can be tracked by its length, a_c. The adhesive crack, on the other hand, is not circular. As shown in Figure 26, the adhesive crack extends further between two ridges of the indenter than along the ridges. To characterize the propagation of the adhesive crack, we track both the extent of delamination along the symmetry plane, $a_{a,sym}$, and the extent of delamination along the channel crack, $a_{a,crack}$. Figure 27 shows the length of the respective cracks

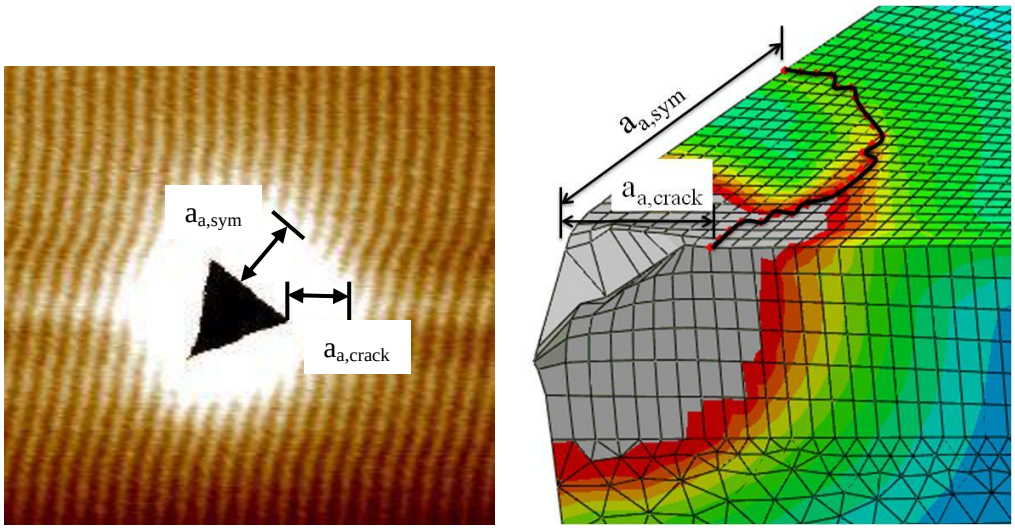

Figure 26: Extent of delamination along the channel crack and symmetry plane a) experimental b) numerical

versus indentation depth for different values of the adhesive fracture energy Γ_a prescribed in the cohesive elements. As expected, the length of the channel crack is not affected by varying values of adhesive fracture energy. The extent of delamination along the symmetry plane also behaves as expected with longer cracks at a given depth for lower adhesive fracture energy. The extent of delamination along the crack plane, however, shows some interesting behavior. Delamination in this direction doesn't initiate at this location until well after delamination at the symmetry plane and then propagates at a rate independent of the Γ_a. The reason for this is show in Figure 28, which show the von Mises' stress in the substrate only viewed normal to the channel crack plane. The gray area is the area of plastic deformation and the crack front is marked. The extent of delamination along the channel crack plane is always within the plastic zone while the extent of delamination along the symmetry plane is well away from this area. This means that delamination along the channel crack plane involves large scale yielding which explains the insensitiveness to changes in the adhesive fracture energy prescribed in the cohesive model. The delamination along the symmetry plane is, as predicted by the 2D model, at least initially, fully characterized by the cohesive model.

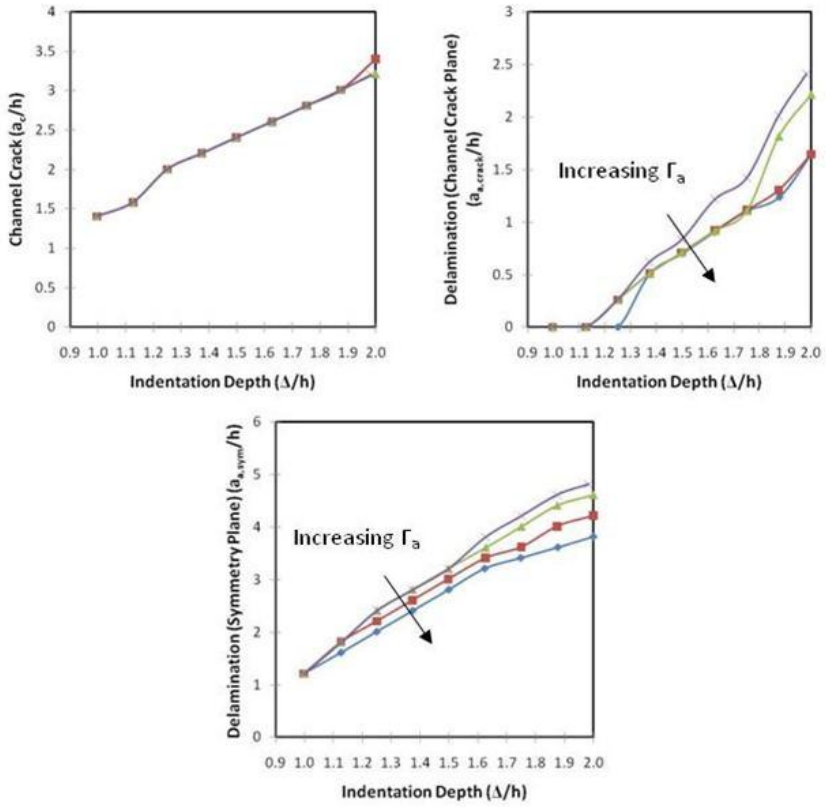

Figure 27: a) Channel crack b) Delamination along channel crack plane c) Delamination along symmetry plane versus depth for various adhesive fracture energies ($\Gamma_a \sim \Gamma_c$)

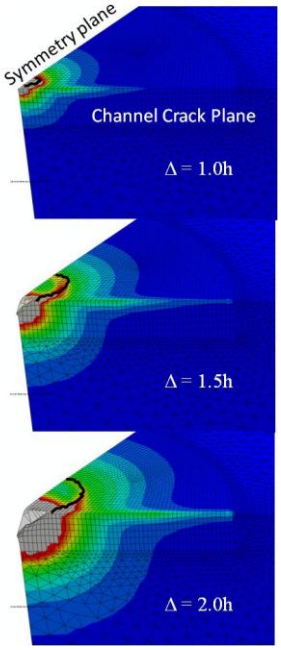

Figure 28: von Mises' stress on the substrate only with delamination marked (black line) at a) $\Delta = 1.0h$ b) $\Delta = 1.5h$ c) $\Delta = 2.0h$

The previous work discussed was done with the adhesive fracture energy and the cohesive energy roughly equal. In the actual material system that has been tested, the cohesive fracture energy is thought to be two orders of magnitude larger than the adhesive fracture energy. Figure 29 shows the cohesive crack lengths for cohesive fracture energies equivalent to $2\,J/m^2$ and $200\,J/m^2$. Surprisingly, there is no difference in cohesive crack length. This implies that something other than fracture energy is the dominant property for this type of fracture. Figure 30 shows the von Mises' stress at various depths for the two cohesive fracture energies. The gray area is the plastic zone. The channel crack front is always within the plastic zone. This means that the cohesive crack is no longer characterized by the cohesive zone model. Evidence of this is also seen in Figure 29, which shows the cohesive crack length increasing due to a relatively small increase (50%) in the yield stress of the film. This implies that cohesive zone models will not be able to extract the cohesive fracture energy from the results of nano-indentation tests.

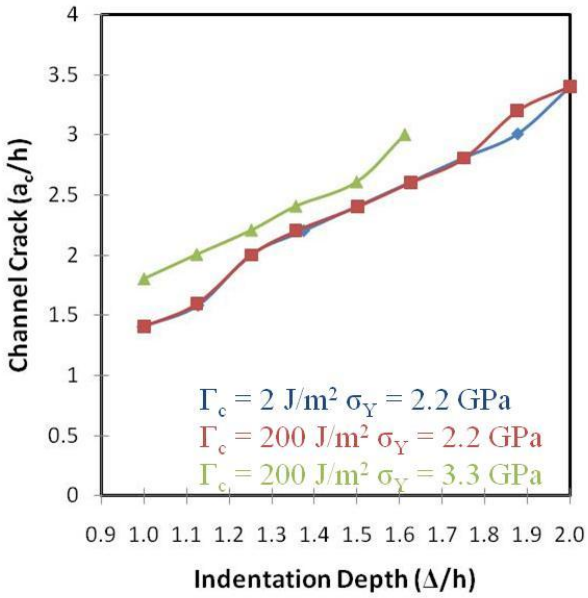

Figure 29: Channel crack length versus indentation depth for two different cohesive fracture energies and two different yield stresses

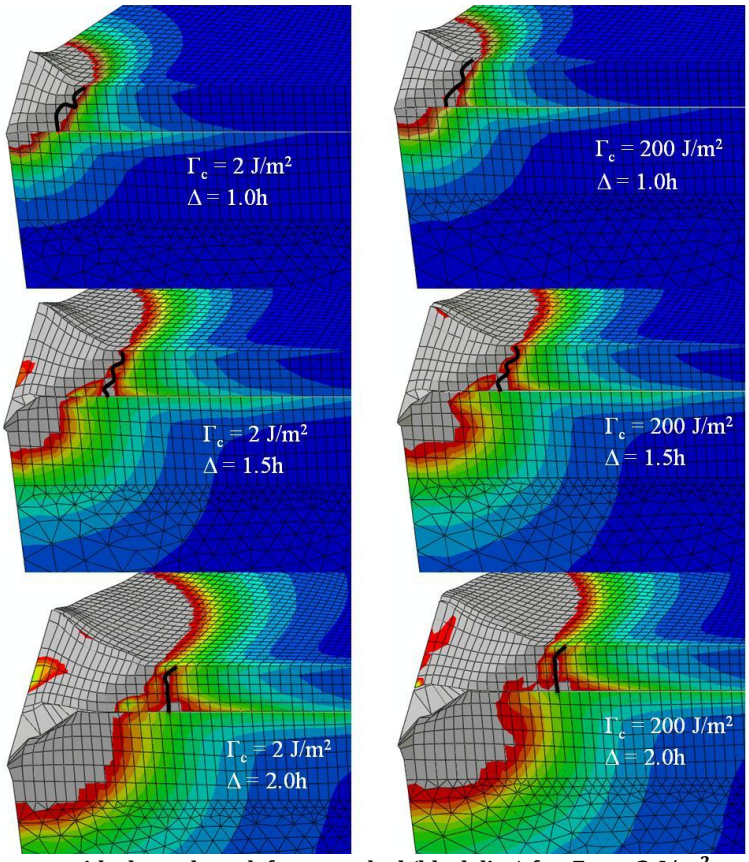

Figure 30: von Mises' stress with channel crack front marked (black line) for $\Gamma_c = 2\,J/m^2$ at a) $\Delta = 1.0h$ b) $\Delta = 1.5h$ c) $\Delta = 2.0h$ and $\Gamma_c = 200\,J/m^2$ at c) $\Delta = 1.0h$ d) $\Delta = 1.5h$ e) $\Delta = 2.0h$

Figure 31 show the extent of delamination along the crack plane and symmetry plane respectively. The two trials are the exact same except for the cohesive stress limit (σ_0) of the traction-separation law in the adhesive cohesive zone. Since the differences in the propagation rate for a given cohesive stress limit are small (less than 5%), if the cohesive stress limit is incorrectly assumed, extremely inaccurate fracture energies can be found. In other words, by varying the cohesive stress limit for a given fracture energy, nearly any crack length can be found at a given indentation depth. This means that the cohesive stress limit must also be known in order to accurately model a given system. Since, at the time of this writing, there is no experimental method to determine the cohesive stress limit for films on the nanometer scale, it is deemed that there are too many unknowns to use cohesive zone modeling to determine the fracture energy in this experiment.

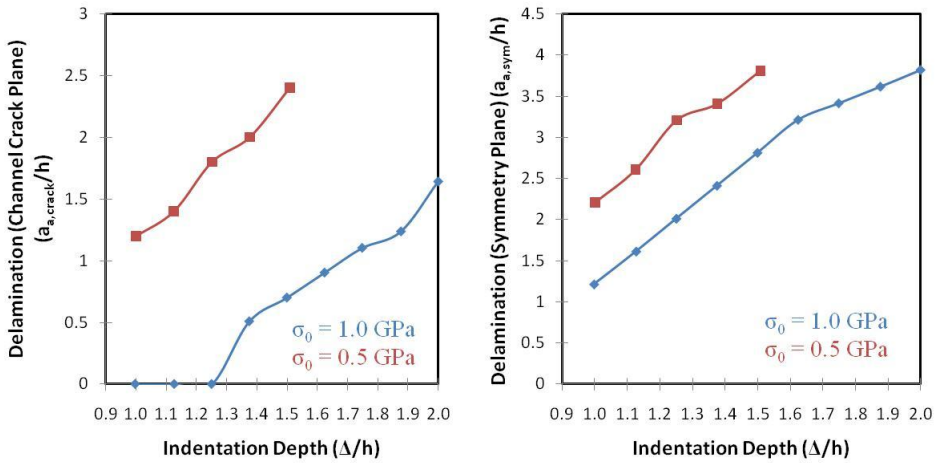

Figure 31: Delamination along a) the channel crack plane and b) the symmetry plane for different initial stresses in the adhesive traction - separation law

Static Model

Since cohesive zone modeling has too many variables to the fracture energy, it was thought to try a purely static model. In static crack modeling, the system is modeled with a predetermined crack length and then loaded. A series of force-displacement curves, such as those in Figure 32, can be created by modeling a range of crack lengths. The work done during an excursion at a given load can then easily be found by finding the difference in displacement between two crack lengths at a given load multiplied by the load. After substituting Equation (3.2) into Equation (3.1), Equation (3.1) can be rewritten as

$$\delta W\left(1+\frac{\delta U_e-\delta W_p}{\delta W}\right)=\Gamma_c\delta a_c+\Gamma_a\delta a_a \tag{4.3}$$

Find the non-fracture energy ratio $(\delta U_e-\delta W_p)/\delta W$ and the total fracture energy for a given excursion can be calculated.

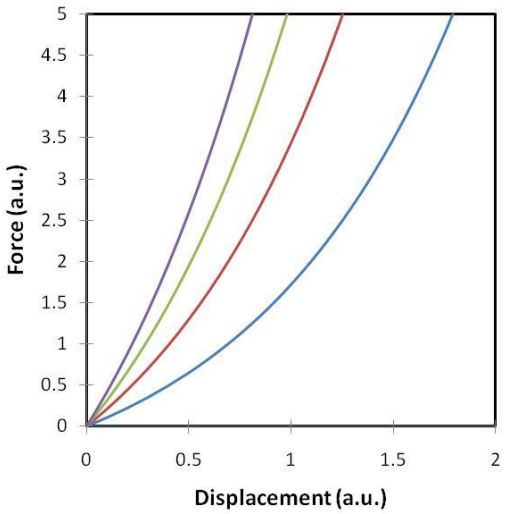

Figure 32: Example force-displacement curves

Figure 33 shows the force versus indentation depth for a variety of cracked systems. Some contain only channel cracks; some contain only adhesive cracks; and some contain both crack types. As can be seen, there is no discernable pattern in the deviation from the non-cracked system other than longer cracks, larger total crack area, produce larger deviations. This implies that an excursion of a known width could be caused by propagation of a channel crack, delamination, or a combination of the two and there is no method to determine the source. By comparing the depth at a given force, the work done by an excursion between two states can be found. Using Figure 34, and the depth at the onset of the excursion, the difference in strain energy and plastic dissipation between the two states can be found. However, Figure 34a reveals an interesting trend. While all of the cracked systems are more compliant than the non-cracked system, some of them still have higher strain energy. The strain energy increases because there is a lower stress concentration near that indenter due to the applied load being spread over a larger area. This delays yielding and allows the system to absorb more energy elastically. In all propagating crack systems, the strain energy was always lowered. This discrepancy implies that the large plastic deformation during indentation is path dependent and therefore cannot be analyzed statically.

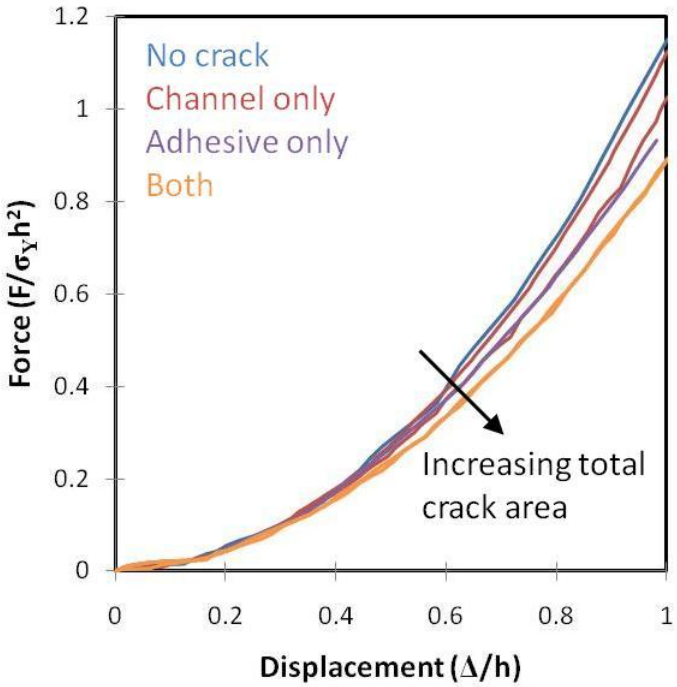

Figure 33: Force - displacement curves for a variety of cracked systems

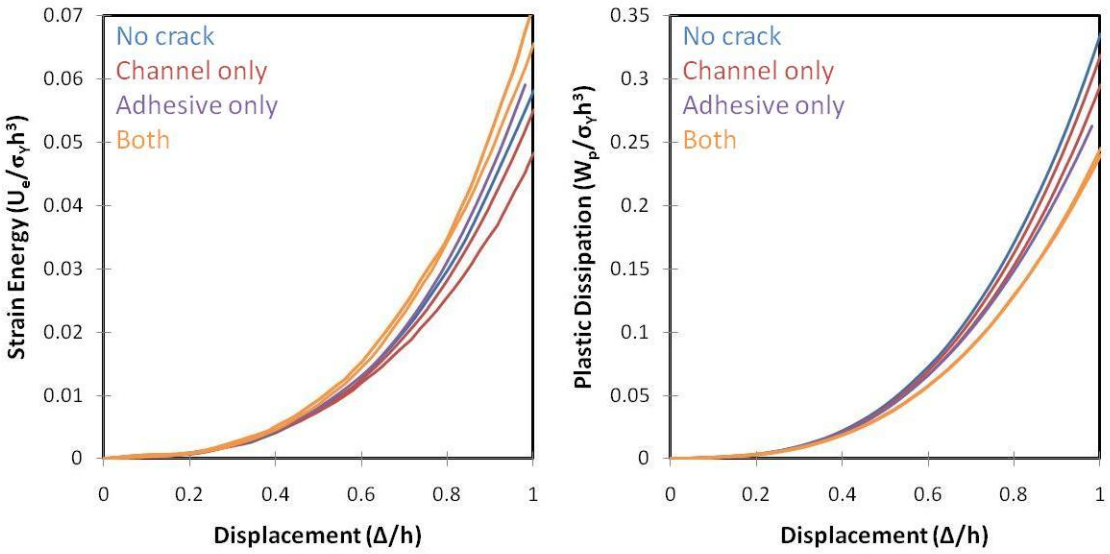

Figure 34: a) Strain energy and b) plastic dissipation for various cracked systems

Conclusion

In conclusion, several models were created to study fracture during nano-indentation. The first was a two dimensional, axisymmetric model capable of propagating only delamination of the film from the substrate. This model was used to study cohesive zone modeling, verify experimental testing procedures,

and develop experimental testing limits. It was found that the extent of delamination must be larger than twice the indentation depth and that the indentation must be at least through the film to insure valid results. Next, a one-sixth three dimensional model capable of propagating both delamination and channel cracks was created. This model shows that the channel crack is always within the elastic-plastic fracture mechanics regime, hindering the use of cohesive zone models in determining the fracture energy. It was also determined that the cohesive stress limit in the delamination traction-separation law played a large role in determining the extant of delamination. This means that there are too many unknowns to currently calibrate the model to a given experimental system. Therefore, a static three dimensional model was developed. A variety of crack combinations were tested. It was determined that indentation is path dependent and cannot be analyzed by a combination of static systems. This means that a method of determining the cohesive strength of ultra thin films needs to be found before the propagating crack model can be matched to a specific film-substrate system.

Chapter 5) Conclusion

Several models were created to study fracture during nano-indentation. Nano-indentation is simply an extension of standard indentation experiments into the nanometer range. Due to the small size of the residual indentations, contact area is indirectly measured from the indentation depth instead of directly measured as in conventional indentation tests. The principles of contact mechanics are the driving theory behind all indentation tests. Nano-indentation can be used to examine more material properties than just hardness and elastic modulus such as elastic-plastic properties, fracture toughness, and strain hardening. Cohesive zone models are used to model crack propagation along a known path. They do this by confining the fracture process zone into a line or plane of zero thickness elements along the path of fracture. These elements use a traction-separation law that decays after the cohesive strength limit of the material is reached. The fracture energy, cohesive strength limit, and, possibly, the form of the traction-separation law are needed to match the cohesive zone model to a given material. The first model was a two dimensional, axisymmetric model capable of propagating only delamination of the film from the substrate. This model was used to study cohesive zone modeling, verify experimental testing procedures, and develop experimental testing limits. It was found that the extent of delamination must be larger than twice the indentation depth and that the indentation must be at least through the film to insure valid results. Next, a one-sixth three dimensional model capable of propagating both delamination and channel cracks was created. This model shows that the channel crack is always within the elastic-plastic fracture mechanics regime, hindering the use of cohesive zone models in determining the fracture energy. It was also determined that the cohesive stress limit in the delamination traction-separation law played a large role in determining the extant of delamination. This means that there are too many unknowns to currently calibrate the model to a given experimental system. Therefore, a static three dimensional model was developed. A variety of crack combinations were tested. It was determined that indentation is path dependent and cannot be analyzed by a combination of static systems. This means that fracture during indentation can be modeled and the trends analyzed, as was done in this study, but a specific film-

substrate systems fracture toughness cannot be determined without previously knowing its cohesive strength.

Bibliography

1. Measurement of fracture toughness of ultra-thin amorphous carbon films. Li, Xiadong and Bhushan, Bharat. 1-2, s.l. : Thin Solid Films, 1998, Vol. 315.

2. Fracture toughness, adhesision and mechanical properties of low-K dielectric thin films measured by nanoindentation. Volinsky, Alex A., Vella, Joseph B. and Gerberich, William W. 1-2, s.l. : Thin Solid Films, 2003, Vol. 429.

3. Indentation fracture toughness and acoustic energy release in tetrahedral amorphous carbon diamond-like thin films. Jungk, J. M., et al. s.l. : Acta Materialia, 2006, Vol. 54.

4. Fisher-Crips, Anthony C. Nanoindentation. New York : Springer - Verlag, 2004.

5. An improved technique for determining hardness and elastic modulus using load and displacement sensing indentation experiments. Olliver, W. C. and Pharr, G. M. 6, s.l. : Journal of Materials Research, 1992, Vol. 7.

6. Experimental investigation of the Sneddon solution and an improved solution for the analysis of nanoindentation dta. Hay, Jack C. and Pharr, G. M. s.l. : Materials Research Society Symposium Proceedings, 1998.

7. Nano-indentation of copper thin films on silicon substrates. Suresh, S., Nieh, T.-G. and Choi, B. W. 9, s.l. : Scripta Materialia, 1999, Vol. 41.

8. Effects of the substrate on the determination of thin film mechanical properties by nanoindentation. Saha, Ranjana and Nix, William D. 23-38, s.l. : Acta Materialia, 2002, Vol. 50.

9. Load-displacement relations for nanoindentation of viscoelastic materials. Liu, Chien Kuo, et al. 3, s.l. : Journal of Applied Physics, 2006, Vol. 100.

10. Strain hardening and recovery in a bulk metallic glass under nanoindentation. Yang, Bing, Riester, Laura and Nieh, T. G. 7, s.l. : Scripta Materialia, 2006, Vol. 54.

11. Hertz, H. On the contact of elastic solids. Hertz's Miscellaneous Papers. London : Macmilllan & Co., 1896.

12. Boussinesq's problem for a rigid cone. Sneddon, I. N. 4, s.l. : Proceedings of the Cambridge Philosophical Society, 1948, Vol. 44.

13. Instrumentaion: Hysitron TI 750 Ubi Nanoindenter. University of Nebraska - Lincoln: BM3L. [Online] University of Nebraska - Lincoln. [Cited: April 30, 2011.] http://www.engineering.unl.edu/research/bm3/Nanoindenter.shtml#details.

14. Anderson, T.L. Fracture Mechanics: Fundamentals and Applications. Boca Raton, FL : Taylor & Francis Group, 2005.

15. Shank, M. E. A critical review of brittle failure in carbon plate steel structures other than ships. Washington, D.C. : National Academy of Science - National Research Council, 1953.

16. Investigation of structrual failures of welded ships. Williams, M. L. and Ellinger, G. A. s.l. : Welding Journal, 1953, Vol. 32.

17. Stresses in a plate due to the presence of cracks and sharp corners. Inglis, C. E. s.l. : Transactions of the Institute of Naval Architects, 1913, Vol. 55.

18. The phenomena of rupture and flow in solids. Griffith, A. A. s.l. : Philosophical Transactions, 1920, Vol. 221.

19. Fracture Dynamics. Irwin. Cleveland, OH : American Society of Metals, 1948.

20. Onset of fast crack propatation in high strength seel and aluminum alloys. Irwin, G. R. s.l. : Sagamore Research Conference Proceedings, 1956.

21. The mathematical theory of equilibrium cracks in brittle fracture. Barenblatt, G.I. s.l. : Advances in Applied Mechanics, 1962, Vol. 7.

22. Yielding of steel sheets containing slits. Dugdale, D. 2, s.l. : Journal of Mechanics and Physics of Solids, 1960, Vol. 8.

23. Analysis of crack formation and crack growth in concrete by means of fracture mechanics and finite elements. Hillerborg, A., Modeer, M. and Petersson, P.-E. 6, s.l. : Cement and Concrete Research, 1976, Vol. 6.

24. Numerical aspects of cohesive-zone models. de Borst, Rene. 14, s.l. : Engineering Fracture Mechanics, 2003, Vol. 70.

25. An analysis of tensile decohesion along an interface. Needleman, A. 3, s.l. : Journal of Mechanics and Physics of Solids, 1990, Vol. 38.

26. Impact-induced delamination of composites: a 2D simulation. Geubelle, Philippe H. and Baylor, Jeffrey S. 5, s.l. : Composites Part B: Engineering, 1998, Vol. 29.

27. Some issues in the application of cohesive zone models for metal-ceramic interfaces. Chandra, N., et al. 10, s.l. : International Journal of Solids and Structures, 2002, Vol. 39.

28. Measuring the fracture toughness of ultra-thin films with application to AlTa coatings. Xiang, Yong, et al. 3, s.l. : International Journal of Fracture, 2007, Vol. 144.

29. Unstable crack propagation in metals: cleavage and fast fracture. Wells, A. A. Cranfield, UK : Proceedings of the Crack Propagation Symposium, 1961.

30. A path independent integral and the approximate analysis of strain concentration by notches and cracks. Rice, J. R. s.l. : Journal of Applied Mechanics, 1968, Vol. 35.

31. Plane strain deformation near a crack tip in a power-law hardeing material. Rice, J. R. and Rosengren, G. F. s.l. : Journal of the Mechanics and Physics of Solids, 1968, Vol. 16.

32. Singular behavior at the end of a tensile crack tip in a hardening material. Hutchinson, J. W. s.l. : Journal of the Mechanics and Physics of Solids, 1968, Vol. 16.